

The long road to the Green Valley: Tracing the evolution of the Green Valley galaxies in the EAGLE simulation

Apashanka Das^a and Biswajit Pandey^a

^aDepartment of Physics, Visva-Bharati University, Santiniketan, 731235, India

E-mail: a.das.cosmo@gmail.com, biswap@visva-bharati.ac.in

Abstract. We study the evolution of the progenitors of the present-day Green Valley (GV) galaxies across redshift $z = 10 - 0$ using data from the EAGLE simulations. We identify the present-day green valley galaxies using entropic thresholding and track the evolution of the physical properties of their progenitors up to $z = 10$. Our study identifies three distinct phases in their evolution: (i) an early growth phase ($z = 10 - 6$), where progenitors are gas-rich, efficiently form stars, and experience AGN feedback regulating star formation in massive galaxies, (ii) a transition phase ($z = 6 - 2$), marked by frequent interactions and mergers in higher-density environments, driving starbursts, depleting gas reservoirs, and strengthening correlations between cold gas and halo properties, and (iii) a quenching phase ($z = 2 - 0$), dominated by environmental and mass-dependent processes that suppress star formation and deplete cold gas. Our analysis shows that at $z < 1$, environmental factors and cold gas depletion dominate quenching, with tighter correlations between stellar mass, SFR, and cold gas content. The interplay between mass and environmental density during this period drives diverse and distinct evolutionary pathways. Our analysis shows that majority of the main progenitor branches of the present-day GV galaxies entered the green valley at $z < 1$. We also find that a small fraction ($\sim 5\%$) of the main progenitor branches had already crossed the green valley and joined the red sequence by $z = 0.1$, indicating that some galaxies may undergo late-time rejuvenation, that allows them to reenter the green valley by the present day. Our findings provide a comprehensive view of the mechanisms shaping the GV population across cosmic time.

Contents

1	Introduction	1
2	Data and method of analysis	4
2.1	Data	4
2.2	Identifying the present-day green valley galaxies using entropic thresholding	5
2.3	Quantifying the local environment of green valley galaxies and their progenitors	6
2.4	Identifying AGN activity in green valley galaxies and their progenitors	7
2.5	Identifying green valley galaxies and their progenitors in interacting pairs	7
3	Results	8
3.1	AGN activity in the progenitors of the present-day green valley galaxies	8
3.2	Galaxy interactions in the progenitors of the present-day green valley galaxies	9
3.3	Evolution of star formation rate and cold gas mass in the progenitors of the present-day green valley galaxies	9
3.4	Roles of mass and local environment in the evolution of the progenitors of the present-day green valley galaxies	19
3.5	Evolution of the main progenitor branches of the present-day green valley galaxies	20
4	Conclusions and Discussions	23
5	Acknowledgements	26
6	Data availability	26

1 Introduction

The observed galaxy properties exhibits a striking bimodality [1–5], a phenomenon that has captivated astronomers for the last few decades. This bimodality becomes evident when galaxies are plotted on a colour-magnitude or colour-stellar mass diagram, where they distinctly separate into two groups: the blue cloud and the red sequence. The blue cloud consists of star-forming galaxies characterized by ongoing star formation and the presence of young, massive stars. In contrast, the red sequence consists of quiescent galaxies with older stellar populations, whose redder colours indicate minimal or no recent star formation. This dichotomy has profound implications for understanding the processes that drive galaxy evolution over cosmic time.

Deciphering the origins and evolution of this bimodality is crucial for unraveling the mechanisms behind galaxy formation and evolution. Semi-analytic models have been developed to replicate the observed bimodality and provide insights into the underlying physical processes [6–13]. Observations reveal that the colour bimodality of galaxies persists up to a redshift of $z = 1 - 2$ [14–17]. It has been found that the number of massive red galaxies at a fixed stellar mass has steadily increased since $z \sim 1$ [14, 18]. This growth suggests that galaxies in the blue cloud migrate to the red sequence through the quenching of star formation. The red stellar mass may also increase via mergers of already quenched, less massive galaxies. Furthermore, the cosmic star formation rate has declined sharply between $z = 1$ to $z = 0$

[19]. These trends highlight significant changes in galaxy properties in recent cosmic history, which have likely played a pivotal role in shaping the observed bimodality. Collectively, these observations suggest that galaxies undergo a transformation from the blue cloud to the red sequence over time, providing crucial insights into the dynamics of galaxy evolution.

Between the blue cloud and the red sequence lies the enigmatic “green valley” [20], a relatively sparse region that represents a transitional phase in galaxy evolution. Galaxies in the green valley are thought to be quenching their star formation, transitioning from the active star-forming state of the blue cloud to the quiescent state of the red sequence. This phase is significant because it provides a window into the processes that halt star formation, offering critical insights into the balance between growth and decline in the cosmic life-cycle of galaxies.

The distribution of galaxies across the blue cloud, green valley, and red sequence reflects a dynamic interplay of physical processes. Star-forming galaxies in the blue cloud often have ample cold gas reserves fueling star formation. Various environment-driven processes, including mergers [21], harassment [22, 23], strangulation [24, 25], starvation [26–28], and satellite quenching [29], can suppress star formation and alter galaxy structure. Large number of studies using simulations [30–44] and observations [45–60] show that interactions between galaxies produce tidal torques which can trigger starbursts and significantly affect their colour and morphology.

In addition to external factors, internal mechanisms also play a crucial role in quenching star formation. Processes such as morphological quenching [61], mass quenching [62–65], angular momentum quenching [66], and bar quenching [67] can lead to the cessation of star formation. Gas loss, whether through feedback from supernovae, active galactic nuclei, shock-driven winds [68–70], or ram pressure stripping [24], provides another effective route for quenching.

Once galaxies enter the red sequence, they settle into a quiescent phase where significant star formation is unlikely without external disruptions. The journey from the blue cloud through the green valley to the red sequence can take varying amounts of time, depending on the internal and external mechanisms driving the transition. Gradual quenching, such as secular quenching, occurs as galaxies deplete their gas reserves over time without replenishment, often as a result of long-term changes in gas inflow and outflow dynamics. This slow process, sometimes referred to as “natural aging”, can span 1 – 2 Gyr [25, 26, 61]. In contrast, rapid quenching mechanisms, such as mergers and ram pressure stripping, can halt star formation in less than 1 Gyr [24, 71]. The transitional green valley phase is therefore critical for understanding both the timeline and drivers of galaxy transformation. Does quenching occur rapidly or gradually? Are external environmental factors more influential than internal processes? How do the dominant quenching mechanisms evolve with time? Are certain processes more influential at particular cosmic epochs? By studying galaxies in the green valley and their progenitors, one can identify the dominant pathways that shape the bimodal distribution of galaxies.

Precisely defining the green valley has been a persistent challenge in studies of galaxy evolution. Broadly, the green valley is conceptualized as the transitional region between the star-forming blue cloud and the quiescent red sequence on colour-magnitude or colour-stellar mass diagrams. Various methodologies have been proposed to delineate this region. [72] delineate the green valley by employing two empirical lines in the colour-stellar mass diagram. [73] map the green valley within the (NUV–r) colour-stellar mass plane using empirical boundaries, analyzing the characteristics of transitional galaxies across various environments. [74]

classify galaxies into red, blue, and green categories using three broad colour bins derived from point densities in the colour-mass plane. [75] suggest defining the green valley based on the strength of the 4000 break, which was later employed for in-depth studies of stellar populations in green valley galaxies [76]. [77] utilize a fuzzy set theory approach to classify galaxies as red, blue, or green within the SDSS dataset. [78] and [79] utilize this classification to examine the properties of green valley galaxies and red spirals across various environments. [80] reinterpret the green valley by linking galaxy morphology to evolutionary trends, defining it through the average colour of different Hubble types. [81] adopt the NUVrK colour-colour diagram to separate the galaxies in the blue cloud, green valley, and red sequence. [82] define the green valley based on the shape of the $\log(\text{sSFR})$ distribution, investigating the morphological changes of transitional galaxies observed in the CLEAR survey. [83] use empirical lines in the SFR-stellar mass plane to define the green valley, exploring how different environments affect the quenching of these galaxies. The absence of a universal definition complicates the objective study of green valley galaxies and their evolution. The boundaries of the green valley vary depending on the methodology and datasets used.

To address these inconsistencies, [84] propose a parameter-free method using Otsu’s image segmentation technique to distinguish the blue cloud and red sequence. However, this approach does not explicitly identify the green valley. More recently, [85] introduced a method for separating the green valley using entropic thresholding [86, 87], which is based on the principle of maximum entropy. This approach provides a natural and robust definition of the green valley, with boundaries determined solely by the data. By eliminating the need for arbitrary thresholds, this method offers a more general and data-driven framework for studying the green valley.

The journey of galaxies through the “green valley” represents a pivotal phase in their evolution, acting as a bridge between the star-forming “blue cloud” and the quiescent “red sequence”. The primary aim of this study is to explore the journey of galaxies from the star-forming blue cloud to the present-day green valley over cosmic time. Galaxies are dynamic cosmic ecosystems, where star formation is fueled by cold gas and regulated by a delicate balance of internal and external factors. However, this balance can be disrupted, leading to the cessation of star formation, a process known as quenching. Understanding the mechanisms behind quenching is vital for unraveling the evolution of the galaxy population from the early Universe to the present day. Numerous quenching mechanisms have been identified, but they often interact in complex ways, with their significance varying based on type, mass, and environment of galaxies. These processes rarely act in isolation, instead, galaxies frequently experience a combination of quenching influences throughout their lifetimes. The diversity of quenching pathways highlights the intricate nature of galaxy evolution and underscores the importance of detailed investigations, such as those conducted with hydrodynamical simulations, to disentangle the contributions of these mechanisms. Deciphering when and how these processes operate is critical for explaining the observed bimodality in galaxy populations and understanding the intricate evolutionary pathways that lead galaxies through the green valley.

Studying the progenitors of present-day green valley galaxies across cosmic time allows us to uncover the physical drivers of star formation quenching and assess their relative importance at different epochs. Hydrodynamical simulations, such as the Evolution and Assembly of Galaxies and their Environments (EAGLE) project [88], provide a powerful tool for this purpose. These simulations capture the complex interplay of gravitational dynamics, hydrodynamic processes, and feedback mechanisms that govern galaxy evolution, enabling detailed tracking of individual galaxy histories. By tracing the progenitors of present-day green val-

ley galaxies from high redshifts ($z = 10$) to the present day ($z = 0$), we can disentangle the cumulative effects of various quenching mechanisms. This comprehensive approach offers a time-resolved perspective on how galaxies gradually lose their capacity to sustain star formation, shedding light on the intricate pathways of galaxy transformation.

The structure of the paper is as follows: Section 2 provides a description of the data and the methodology, Section 3 discusses the results, and Section 4 presents the conclusions.

2 Data and method of analysis

2.1 Data

We utilize data from the EAGLE suite of cosmological hydrodynamical simulations of galaxy formation [88–90]. These simulations model the evolution of both baryonic and dark matter from a starting redshift of $z = 127$ to the present day. The EAGLE simulations are based on a flat Λ CDM cosmological model, with parameters derived from the Planck Mission results [91]. The galaxies are simulated across cosmic time within comoving cubic volumes, with side lengths ranging from 25 to 100 Mpc.

In this study, we use the reference model denoted as *Ref – L0100N1504*, which simulates a total of 2×1504^3 particles within a comoving cubic box with a side length of 100 Mpc. The initial masses assigned to the baryonic and dark matter particles in this model are $1.81 \times 10^6 M_{\text{sun}}$ and $9.70 \times 10^6 M_{\text{sun}}$, respectively. We extract the comoving coordinates of the simulated galaxies, which are identified by the locations of their minimum gravitational potential. Only genuine galaxies are selected by applying the criterion *Spurious* = 0. Additionally, we retrieve various physical properties of these galaxies, such as stellar mass, star formation rate, cold gas mass, dark matter mass, and $(u - r)$ colour. These properties are measured within a 3D spherical aperture of comoving radius 30 kpc centered on the galaxy’s minimum gravitational potential. The $(u - r)$ colour represents the difference in the rest-frame absolute magnitudes of the galaxies in the SDSS u - and r -band filters [92, 93]. At the present-day snapshot ($z = 0$, *Snapnum* = 28), colour information is available only for galaxies with stellar masses $\log(M_{\text{stellar}}/M_{\text{sun}}) \geq 8.3$. Each galaxy in our sample is resolved by at least ~ 110 particles. Combining all this information, we identify a total of 29754 galaxies at $z = 0$.

At $z = 0$, we classify galaxies in our sample as red, blue, or green based on their stellar mass and $(u - r)$ colour, using the entropic thresholding technique described in [subsection 2.2](#). The green galaxies identified in this manner at $z = 0$ include all necessary information, with each galaxy assigned a unique identifier, *GalaxyID*. We use the *GalaxyID* of each green galaxy at $z = 0$ to trace its merger history over past time intervals. In the EAGLE simulation, each galaxy is described by a main progenitor branch, which tracks its individual evolution from $z \sim 10$ to the present day, and by other progenitor branches that record its merger history at different redshifts. The *LastProgID* associated with each green galaxy at $z = 0$ represents the highest *GalaxyID* among all its progenitors across the redshift range from $z \sim 10$ to $z = 0.1$. Thus, for a present-day green galaxy with *GalaxyID* = i and *LastProgID* = j , querying all galaxies with their *IDs* between $i < \text{IDs} \leq j$ across all redshifts retrieves all progenitor galaxies associated with this green galaxy. Following this approach, we identify all progenitor galaxies for green galaxies at $z = 0$. We retrieve the progenitor galaxies of present-day green galaxies in redshift range $z = 10 - 0.1$. Our sample contains 9628 green galaxies at $z = 0$, classified according to the scheme described in [subsection 2.2](#), and a total of 141099 progenitor galaxies. It is important to note that only the green-valley progenitors

with stellar masses $\log(M_{\text{stellar}}/M_{\text{sun}}) \geq 8.3$ are considered in our analysis. This ensures that all the progenitors are resolved by at least 110 particles. This limit in the lower mass is also essential as the colours are only available for the galaxies above this stellar mass in EAGLE simulation.

2.2 Identifying the present-day green valley galaxies using entropic thresholding

We first classify the galaxies as red, blue at $z = 0$ following Otsu's technique proposed in [84]. The method identifies the optimal threshold that separates the bimodal $(u - r)$ colour distribution into two populations, the Blue Cloud (BC) representing star-forming galaxies with younger stellar populations and the Red Sequence (RS) representing passive galaxies with older stellar populations.

The threshold maximizes the inter-class variance and minimizes the intra-class variance. Mathematically, the intra-class variance σ_{intra}^2 and inter-class variance σ_{inter}^2 are expressed as,

$$\sigma_{\text{intra}}^2 = P_{BC}\sigma_{BC}^2 + P_{RS}\sigma_{RS}^2,$$

$$\sigma_{\text{inter}}^2 = P_{BC}P_{RS}(\mu_{BC} - \mu_{RS})^2,$$

where P_{BC} and P_{RS} are the probabilities of class occurrences, and μ_{BC} , μ_{RS} , σ_{BC}^2 and σ_{RS}^2 are the class means and class variances for the two populations.

The green valley is defined as the transitional region between the blue cloud and red sequence. The optimal colour threshold in Otsu's method divides the entire population into blue cloud and red sequence. However this does not help us to identify the green valley sandwiched between the blue cloud and the red sequence. We next classify the galaxies into three distinct classes as red, blue and green following the technique proposed in [85], based on entropic thresholding [87]. We apply entropic thresholding to identify green valley galaxies at $z = 0$. The entire population is first divided into three separate classes $(u - r) \leq \mu_{BC}$, $(u - r) \geq \mu_{RS}$ and $\mu_{BC} < (u - r) < \mu_{RS}$. Here μ_{BC} , μ_{RS} respectively represents the mean colours associated with the blue cloud and red sequence identified with the Otsu's method. The populations with $(u - r) \leq \mu_{BC}$ belongs to the blue cloud and $(u - r) \geq \mu_{RS}$ belongs to the red sequence, and the intermediate region $\mu_{BC} < (u - r) < \mu_{RS}$ is represented by the blue, green and red galaxies. The intermediate region $(\mu_{BC} < (u - r) < \mu_{RS})$ is divided into N bins. Entropic thresholding is employed to partition this region into three distinct zones belonging to Blue Cloud (BC), Green Valley (GV), and Red Sequence (RS). This is achieved by maximizing the total entropy H_{total} of this region

$$H_{\text{total}} = H_{BC} + H_{GV} + H_{RS} \quad (2.1)$$

Here the entropy associated with each class H_{BC} (blue cloud), H_{GV} (green valley), H_{RS} (red sequence) is given by,

$$H_{BC} = \log\left(\sum_{i=1}^{s_1} p_i\right) - \frac{\sum_{i=1}^{s_1} p_i \log p_i}{\sum_{i=1}^{s_1} p_i} \quad (2.2)$$

$$H_{GV} = \log\left(\sum_{i=s_1+1}^{s_2} p_i\right) - \frac{\sum_{i=s_1+1}^{s_2} p_i \log p_i}{\sum_{i=s_1+1}^{s_2} p_i} \quad (2.3)$$

$$H_{RS} = \log\left(\sum_{i=s_2+1}^N p_i\right) - \frac{\sum_{i=s_2+1}^N p_i \log p_i}{\sum_{i=s_2+1}^N p_i} \quad (2.4)$$

Here p_i represents the probability of the i^{th} colour bin, and we choose $N = 30$ bins for our analysis. Previous studies indicate that the boundaries of the green valley defined by entropic thresholding are not significantly sensitive to the choice of the number of bins [85]. The thresholds s_1 and s_2 represent possible colour values between μ_{BC} and μ_{RS} . To identify these thresholds, we iterate over all possible combinations of s_1 and s_2 (with $s_1 < s_2$) in the range $[\mu_{BC}, \mu_{RS}]$ and determine the values that maximize the total entropy, $H_{\text{total}} = H_{BC} + H_{GV} + H_{RS}$. The optimal thresholds s_1 and s_2 thus obtained partition the population into three distinct classes: the Blue Cloud ($(u-r) \leq s_1$), the Red Sequence ($(u-r) \geq s_2$), and the Green Valley ($s_1 < (u-r) < s_2$).

To account for the dependence of galaxy colour on stellar mass, we separately apply this classification process within independent stellar mass bins. Within each bin, we first determine the mean colours μ_{BC} and μ_{RS} for the blue cloud and red sequence using Otsu's technique [84]. We then separate the Green Valley (GV) by identifying two thresholds (s_1, s_2) within μ_{BC} and μ_{RS} , using entropic thresholding [85]. This ensures that the boundaries of the green valley vary dynamically with stellar mass, providing a nuanced classification.

The left panel of Figure 1 illustrates this classification, where the cross points indicate the thresholds s_1 and s_2 for each mass bin, and the solid line represents a smooth cubic polynomial fit to these thresholds in the colour-stellar mass plane. The right panel of Figure 1 shows the PDF of $(u-r)$ colour for the red, blue, and green galaxy populations, classified using the entropic thresholding technique at $z = 0$.

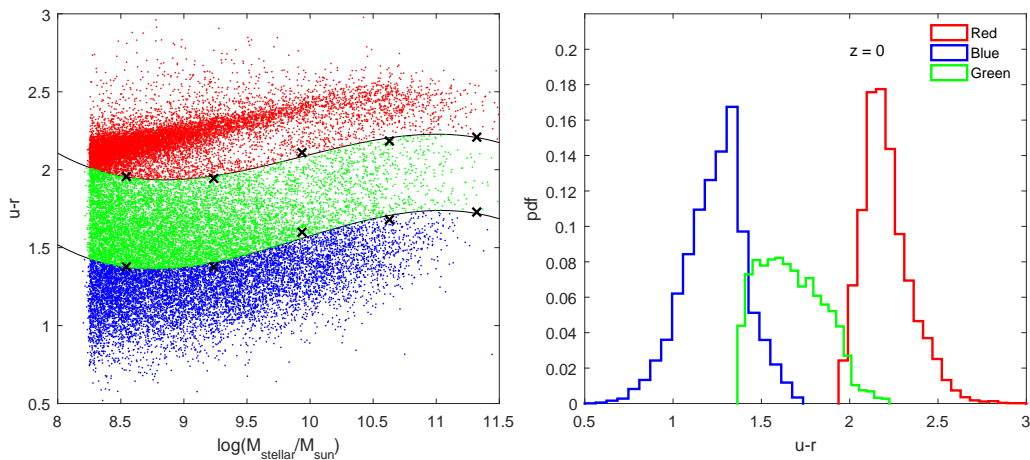


Figure 1. The left panel illustrates red, blue, and green galaxies classified in the colour-stellar mass plane using the entropic thresholding technique. Black cross markers indicate the boundaries of the green valley across different stellar mass bins, with the solid black line representing a cubic polynomial fit to these points. The right panel displays the PDF of $(u-r)$ colour for red, blue, and green galaxies, also classified using entropic thresholding. Both panels correspond to redshift of $z = 0$.

2.3 Quantifying the local environment of green valley galaxies and their progenitors

We quantify the local environment of present-day green valley galaxies and their progenitors by estimating their local density using the method described in [94]. This approach calculates

the local density η_k of a galaxy based on the distance to its k^{th} nearest neighbour as,

$$\eta_k = \frac{k-1}{\frac{4}{3}\pi r_k^3}. \quad (2.5)$$

Here, r_k denotes the distance to the k^{th} nearest neighbour, and the denominator represents the volume of a sphere with radius r_k centered on the galaxy. For our analysis, we calculate the local density (Equation 2.5) using the distance to the 5th nearest neighbour ($k = 5$). Since the EAGLE simulation is conducted within a finite volume with well-defined boundaries, the local density for galaxies near the boundary can be underestimated. This underestimation occurs because some portion of the measuring spheres can lie outside the simulation boundary. To address this issue, we exclude the galaxies from our sample if $r_5 > r_b$, where r_5 represents the distance to the 5th nearest neighbour and r_b represents the distance of the galaxy from the nearest boundary. We consider the entire snapshot at each redshift for determining the local density for the green valley galaxies and their progenitors.

2.4 Identifying AGN activity in green valley galaxies and their progenitors

The presence of an active galactic nucleus (AGN) significantly impacts star formation in a galaxy. When a supermassive black hole accretes material, it converts the gravitational energy of the infalling matter into radiative energy. This radiative energy is emitted into the interstellar medium, disrupting the cold gas reservoirs that are essential for sustaining star formation. The radiation, winds, and jets from the AGN can expel cold gas or heat it, a process known as AGN feedback.

Galaxies actively forming stars can transition to quiescence due to AGN activity, and their emission line flux ratios can be used to distinguish between star-forming and AGN-active galaxies [95]. AGN-active galaxies are characterized by strong emission lines compared to other galaxies. In this study, we classify AGN-active galaxies among the present-day green valley population and their progenitors in the EAGLE hydrodynamical simulation using a luminosity threshold, following the approach outlined in [96]. Galaxies with a bolometric AGN luminosity of $L_{bol} \geq 10^{43}$ erg/s are classified as AGN-active.

The bolometric AGN luminosity is calculated as $L_{bol} = \epsilon_r \dot{m}_{BH} c^2$, where $\epsilon_r = 0.1$ is the radiative efficiency of the accretion disk [97], \dot{m}_{BH} is the black hole accretion rate, and c is the speed of light. This formula represents the fraction of the black hole's accreting mass that is converted into radiative energy. In Figure 2, we present the fraction of green valley galaxies at $z = 0$ and their progenitors at various redshifts that host an AGN.

2.5 Identifying green valley galaxies and their progenitors in interacting pairs

We identify galaxies involved in interactions using the criteria outlined in [98]. A galaxy is classified as interacting if its first nearest neighbour lies within a distance of $r \leq 200$ kpc, where r represents the three-dimensional comoving separation in real space between the locations of the minimum gravitational potential of the galaxies. Using this approach, we determine which green valley galaxies in our sample at $z = 0$ are undergoing interactions. Similarly, we identify progenitor galaxies that are part of interacting pairs at various redshifts. It is worthwhile to mention that we only focus on interacting galaxy pairs with a stellar mass ratio within the range $1 \leq \frac{M_1}{M_2} \leq 10$. This selection ensures that the interactions have a significant impact on both galaxies involved. While galaxy pairs with more extreme mass ratios, such as 1 : 1000, exist in our sample, their interactions are unlikely to meaningfully affect the more

massive galaxy in the pair and are therefore excluded from this study. We show the fraction of present-day green valley galaxies and their progenitors involved in interacting systems in [Figure 3](#). We use the entire snapshot at each redshift for identifying the green valley galaxies and their progenitors in interacting pairs.

3 Results

In this section, we analyze the physical properties of the green valley progenitors across the redshift range $10 - 0.1$ and explore the physical mechanisms and processes driving their evolution.

3.1 AGN activity in the progenitors of the present-day green valley galaxies

To understand the role of AGN feedback in the evolution of GV progenitors, we calculate the fraction of AGN in these galaxies across the redshift range $z = 10$ to $z = 0$. The results, shown in [Figure 2](#), reveal a steady decline in the AGN fraction, dropping from approximately 12% at $z = 10$ to about 2% at $z = 0$. This trend reflects the decreasing significance of AGN feedback as a driver of galaxy evolution over time.

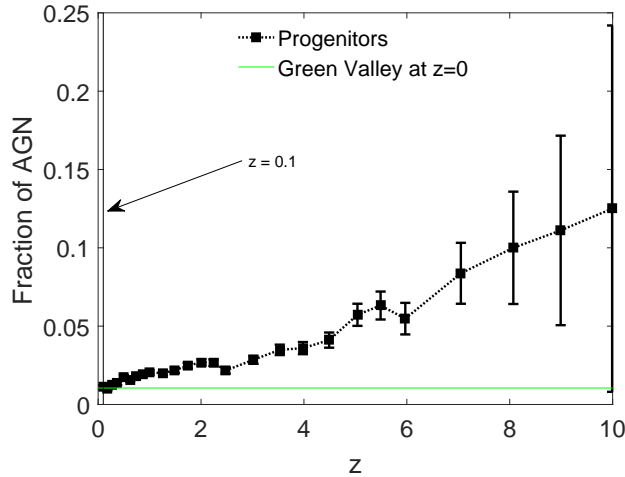


Figure 2. This plot shows the fraction of GV progenitors hosting AGN as a function of redshift. The corresponding fraction for present-day green valley galaxies is indicated by a green horizontal line. Binomial 1σ error bars are shown for each data point.

At low redshifts ($z < 2$), the scarcity of cold gas significantly limited AGN activity, reducing its role in galaxy regulation. At this stage, quenching became primarily driven by environmental factors, secular processes, and lingering effects from earlier AGN feedback. The declining AGN fraction indicates a shift in quenching mechanisms. AGN feedback is most influential during the early stages of quenching but plays a diminished role in maintaining quiescence at later times. As a result, GV progenitors transition from AGN-dominated regulation at high redshifts to quenching dominated by environmental effects and cold gas depletion at lower redshifts.

3.2 Galaxy interactions in the progenitors of the present-day green valley galaxies

We analyze the fraction of interacting galaxies among GV progenitors across the redshift range $z = 10$ to $z = 0$, with results shown in Figure 3. The fraction of interacting galaxies steadily rises from $\sim 5\%$ at $z = 7$ to a peak of $\sim 25\%$ at $z = 2$, before declining to about 19% at the present day.

This trend highlights the significant role of galaxy mergers and interactions in driving galaxy evolution during $2 < z < 7$. Interactions during this period are particularly effective at triggering starbursts and depleting cold gas reservoirs, accelerating the quenching process.

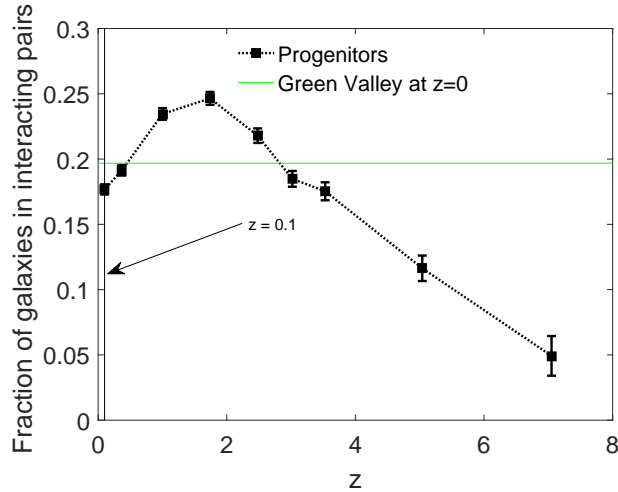


Figure 3. The plot shows the fraction of GV progenitors in interacting galaxy pairs across different redshifts. A green horizontal line indicates the corresponding fraction for present-day green valley galaxies. Binomial 1σ error bars are displayed for each data point.

The frequency of interactions in low-density regions is expected to decrease significantly once the universe entered a phase of accelerated expansion at low redshift. The decline in the interaction fraction at $z < 2$ reflects a shift in quenching mechanisms, with non-interaction-based processes, including environmental effects, secular evolution, and feedback mechanisms, playing an increasingly significant role in shaping the GV population. This evolution underscores the dynamic interplay of interactions and environment in the life cycle of GV progenitors.

3.3 Evolution of star formation rate and cold gas mass in the progenitors of the present-day green valley galaxies

We study the evolution of the star formation rate (SFR) distribution of GV progenitors as illustrated in the panels of Figure 4. This figure compares the SFR distributions of GV progenitors with those of present-day GV galaxies across various redshifts, as indicated in each panel. At higher redshifts ($z \geq 5$), GV progenitors predominantly consist of actively star-forming galaxies. Over time, the peak of the $\log(\text{SFR})$ distribution for GV progenitors gradually shifts to lower values, eventually reaching negative values at redshifts $z \leq 3$. The rate of change in the SFR distribution accelerates at $z < 1$, where the most dramatic decline occurs, signaling a significant suppression of star formation in the GV progenitors.

Since cold gas serves as the essential fuel for star formation, we also track the evolution of cold gas content in GV progenitors over the same redshift range, as shown in Figure 5. A similar trend emerges where GV progenitors at high redshifts were gas-rich, with those at $z \sim 5$ containing, on average, approximately 30 times more cold gas than present-day GV galaxies. However, a steady depletion of cold gas is observed, driven by ongoing star formation and various gas-destroying processes. This depletion becomes most pronounced at $z < 1$, highlighting a strong correlation between the suppression of star formation in GV progenitors and the diminishing availability of cold gas during this period.

We next focus on the stellar mass-SFR relation and halo mass-cold gas mass relation for the GV progenitors to understand their roles in the evolution of SFR and cold gas in these galaxies. The mass of galaxies and their host dark matter halos plays a pivotal role in regulating star formation. A key framework for studying this relationship is the galaxy mass-main sequence, which links stellar mass to the SFR. This correlation reveals that more massive galaxies tend to exhibit higher SFRs, forming a tight and consistent trend across a broad range of stellar masses and redshifts. This pattern arises because stellar mass reflects the capacity of a galaxy to sustain star formation through ongoing gas accretion and the self-regulation of feedback processes. Notably, deviations from the mass-main sequence often signify critical transitions in a galaxy’s life cycle, such as quenching or rejuvenation of star formation. As a result, the mass-main sequence offers valuable insights into the physical mechanisms that drive and suppress star formation throughout cosmic history.

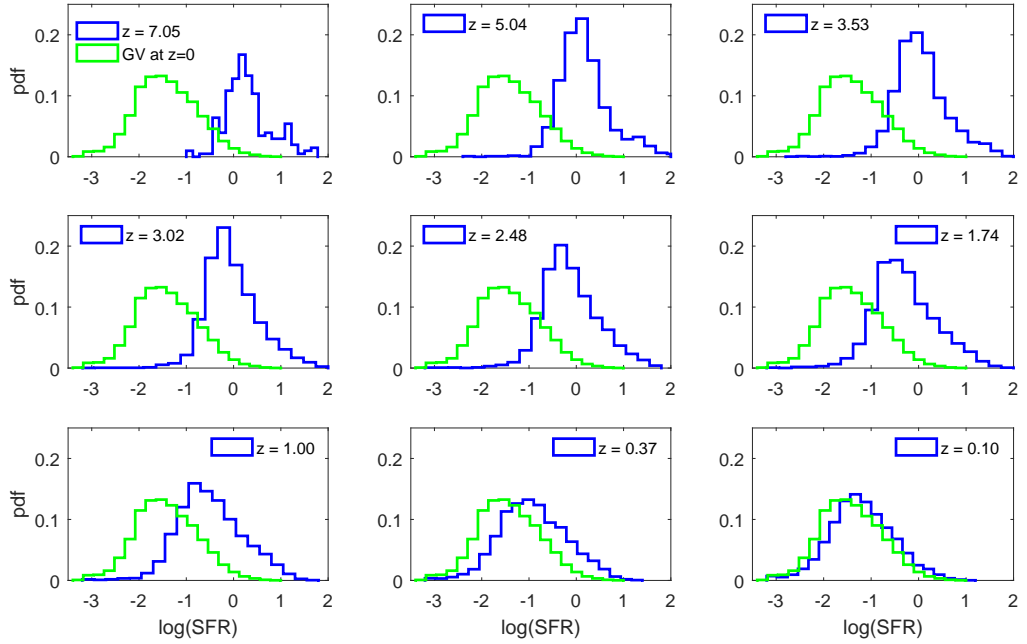


Figure 4. This figure presents the probability distribution of SFR in GV progenitors across different redshifts, with the SFR distribution of present-day green valley galaxies included in each panel for comparison.

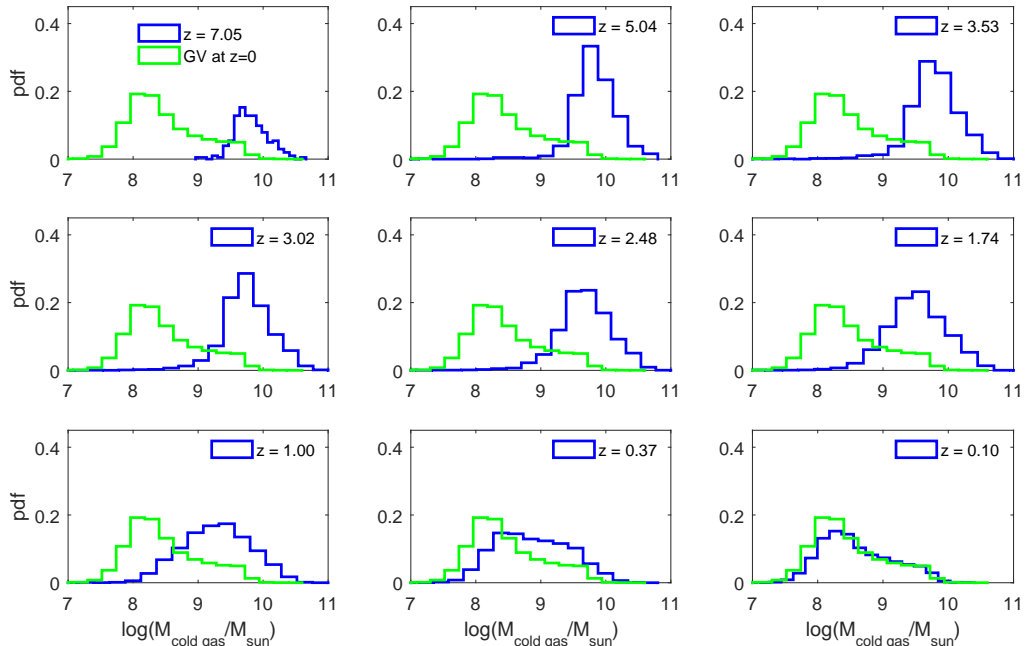


Figure 5. This shows the probability distribution of cold gas mass in GV progenitors at different redshifts. The results for the present-day GV population is shown together in each panel for comparison.

The panels of [Figure 6](#) display the joint PDFs of $\log(\text{SFR})$ and $\log M_{\text{stellar}}$ for GV progenitors across various redshifts, as indicated in each panel. These visualizations clearly reveal the evolution of the main-sequence relation of GV progenitors over time. To quantify this evolution, we calculate the slope of the main-sequence relation at each redshift using a least-squares fitting method. The resulting slopes, plotted as a function of redshift in [Figure 7](#), show distinct trends. The slope decreases from $z = 7$ to $z = 4$, stabilizes between $z = 4$ and $z = 2$, and declines again from $z = 2$ to the present, with the most pronounced changes occurring at $z < 1$.

At high redshifts ($z = 7$ to $z = 4$), star formation is efficient across all stellar masses, driven by an abundance of cold gas and frequent accretion events. As redshift decreases, galaxies of varying masses may quench their star formation through interactions and mergers with neighbouring galaxies. In contrast, the secular processes (e.g. supernova-driven winds) can inhibit star formation in low-mass progenitors. These processes lead to a gradual flattening of the main-sequence slope. Between $z = 4$ and $z = 2$, many progenitors experience a balance between star formation and feedback regulation, maintaining a relatively stable slope.

At $z < 2$, environmental factors begin to dominate. Higher-mass progenitors persist longer in the green valley, particularly in intermediate-density environments, before quenching due to feedback or environmental influences. In contrast, lower-mass progenitors quench earlier and more rapidly, as they are less capable of retaining gas and are more sensitive to feedback effects. By $z < 1$, GV progenitors span a broad range of stellar masses, but most have masses below $10^{10} M_{\text{sun}}$. Consequently, cold gas depletion and environmental factors

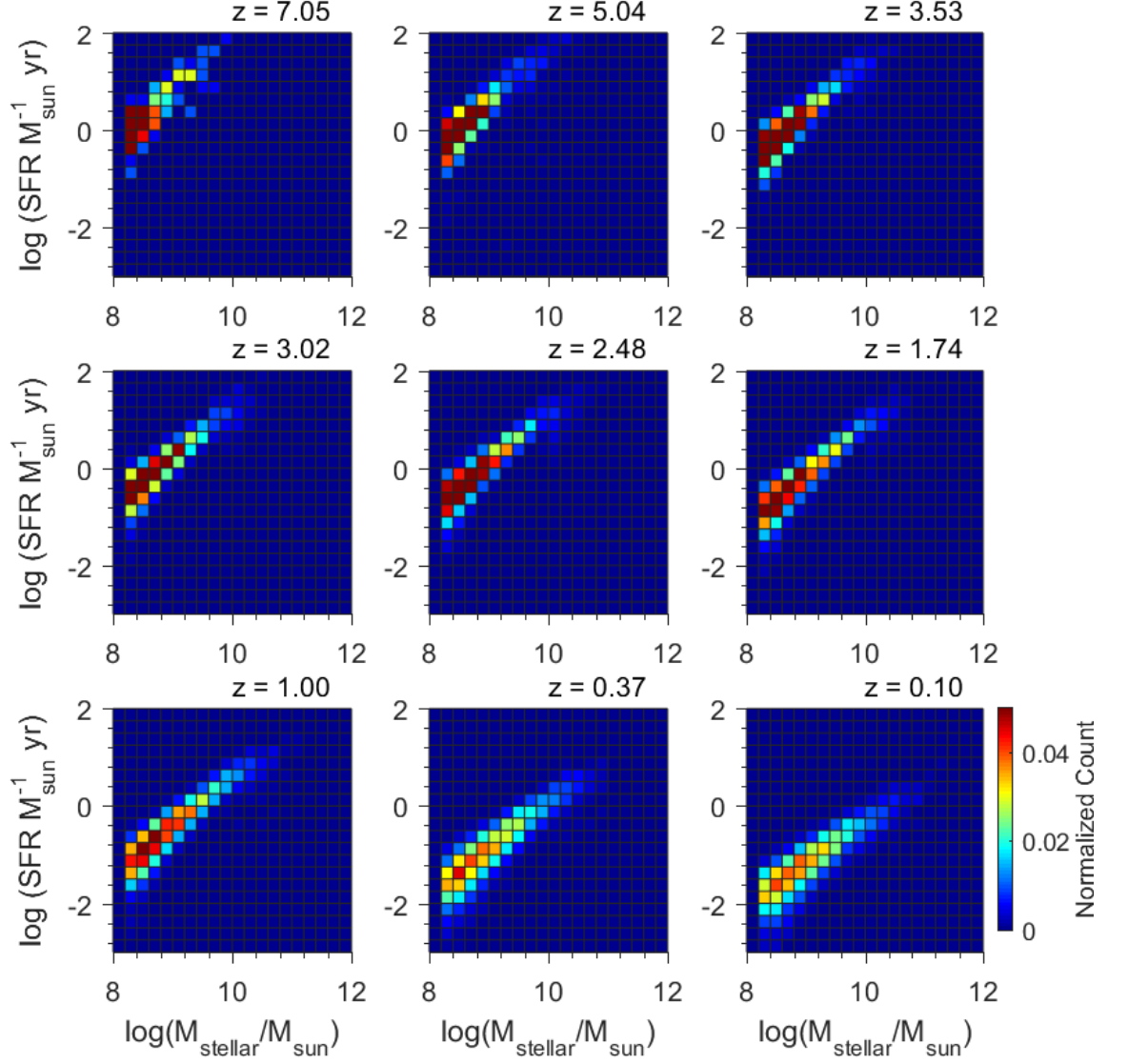


Figure 6. This plot shows the joint PDF of stellar mass and SFR of GV progenitors at different redshifts. The colour bar at the bottom right part of the figure represents the amplitudes of the joint PDF of stellar mass and SFR.

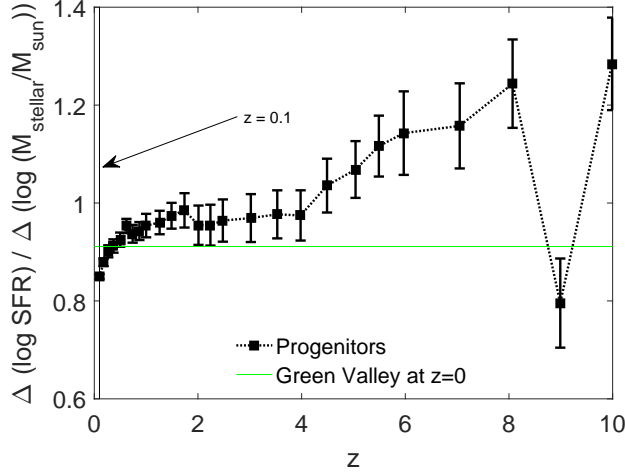


Figure 7. This figure shows the slope of the stellar mass-SFR relation for GV progenitors as a function of redshift. The slope, representing the linear relationship between $\log(M)$ and $\log(SFR)$, is calculated using the least-squares fitting method. The $1-\sigma$ error bars obtained through Jackknife resampling are shown at each data point.

drive the quenching of most GV progenitors, resulting in a dramatic decline in star formation rates at low redshift.

The mass of a galaxy’s dark matter halo plays a pivotal role in regulating its gas reservoir, which directly influences its star formation potential. Massive halos, with their deeper gravitational wells, can retain and accrete more gas from their surroundings while better resisting feedback processes such as supernova-driven outflows. These halos also facilitate the cooling and condensation of hot gas into the cold phase necessary for star formation. In contrast, low-mass halos are more vulnerable to gas loss due to feedback and environmental effects, resulting in smaller gas reservoirs and reduced star formation rates. This intricate interplay between dark matter halo mass and gas dynamics is key to understanding the regulation of star formation, the evolution of galaxies, and the patterns observed in the star-forming main sequence.

The panels in [Figure 8](#) illustrate the joint PDFs of $\log M_{cold\ gas}$ and $\log M_{halo}$ for GV progenitors across various redshifts, as indicated. These panels reveal a strong correlation between cold gas mass and halo mass among GV progenitors. At high redshifts, this correlation is less pronounced, suggesting that cold gas availability in GV progenitors is less tightly regulated by halo mass. This trend likely reflects efficient cold gas accretion from the cosmic web, enabling sustained star formation across a wide range of halo masses.

At lower redshifts ($z < 1$), the correlation steepens significantly, indicating that halo mass becomes a stronger determinant of cold gas availability. This shift may result from the increasing influence of environmental quenching mechanisms at lower redshifts. The cold gas loss from low-mass halos due to feedback or environmental interactions can lead to rapid gas depletion and early quenching of star formation. On the other hand, the high-mass halos may continue to accumulate gas but often experience quenching through mechanisms like virial shock heating or AGN feedback, which prevent the cooling and condensation of gas necessary for star formation. The interplay between halo mass and cold gas dynamics underscores the

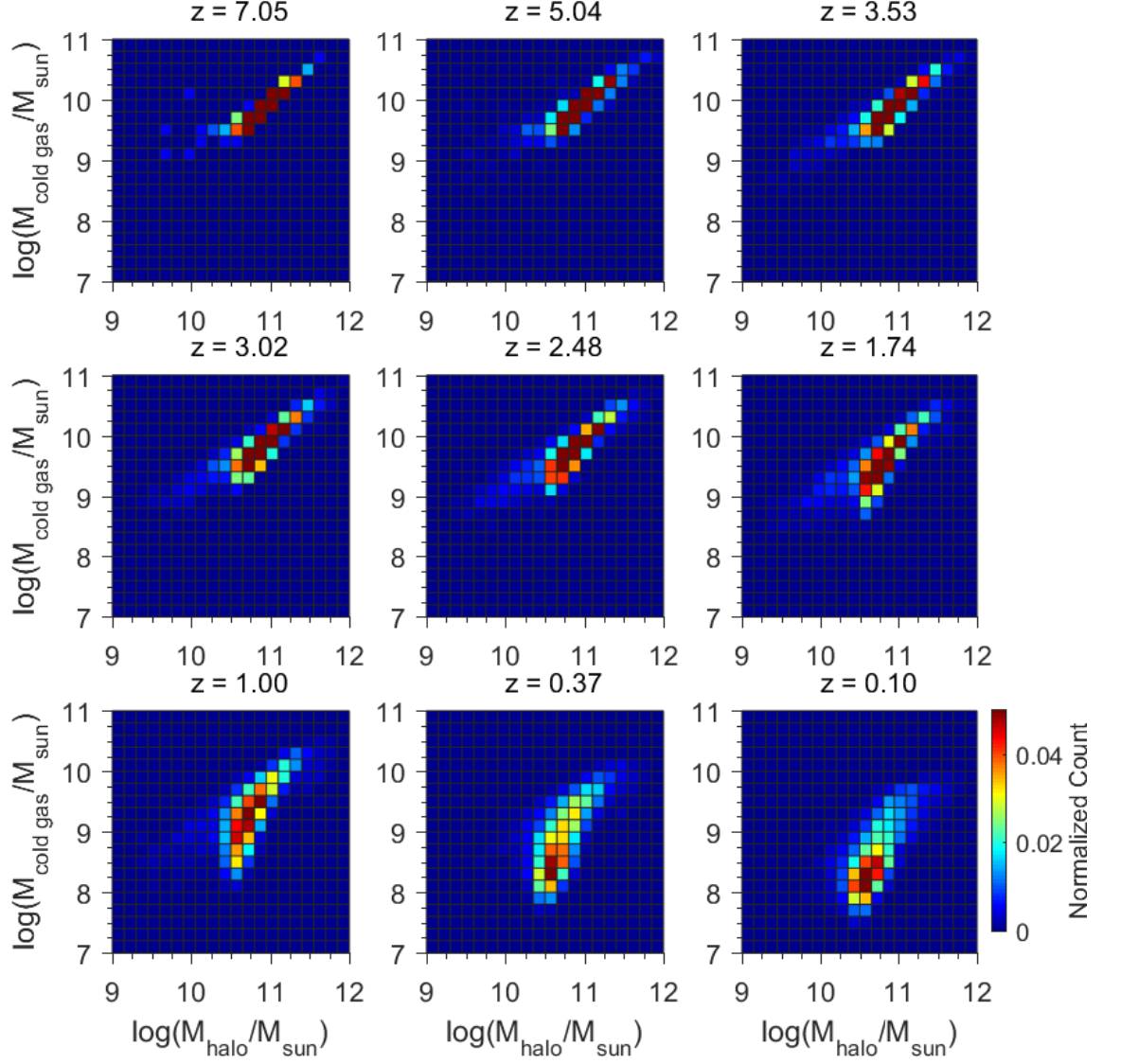


Figure 8. This shows the joint PDF of halo mass and cold gas content of GV progenitors at different redshifts. The colour bar represents the amplitudes of the joint PDF of halo mass and cold gas content.

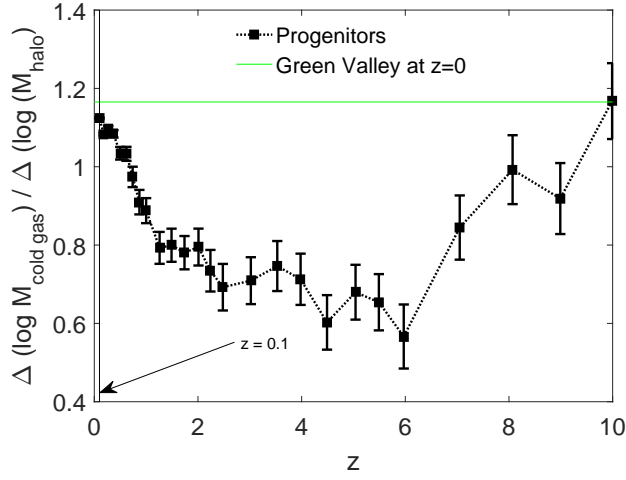


Figure 9. This shows the evolution of the slope of the halo mass-cold gas mass relation for GV progenitors with redshift. We estimate the slope at each redshift using the least-squares fitting method. The $1\text{-}\sigma$ error bars shown at each data point are obtained through Jackknife resampling.

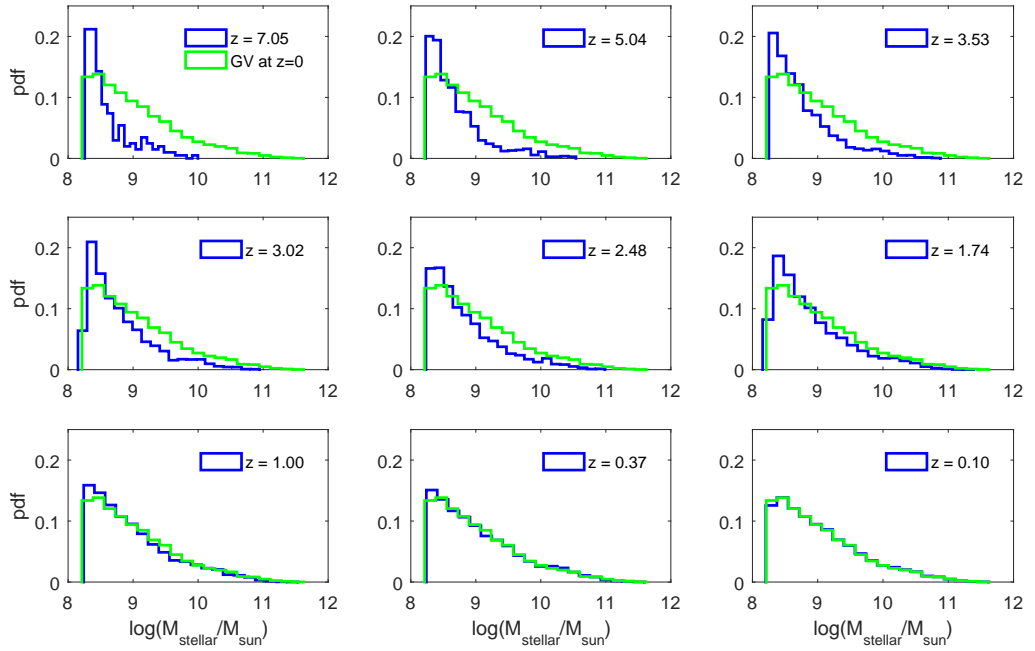


Figure 10. This shows the PDF of the stellar mass for GV progenitors at different redshift along with that for the present-day green valley galaxies.

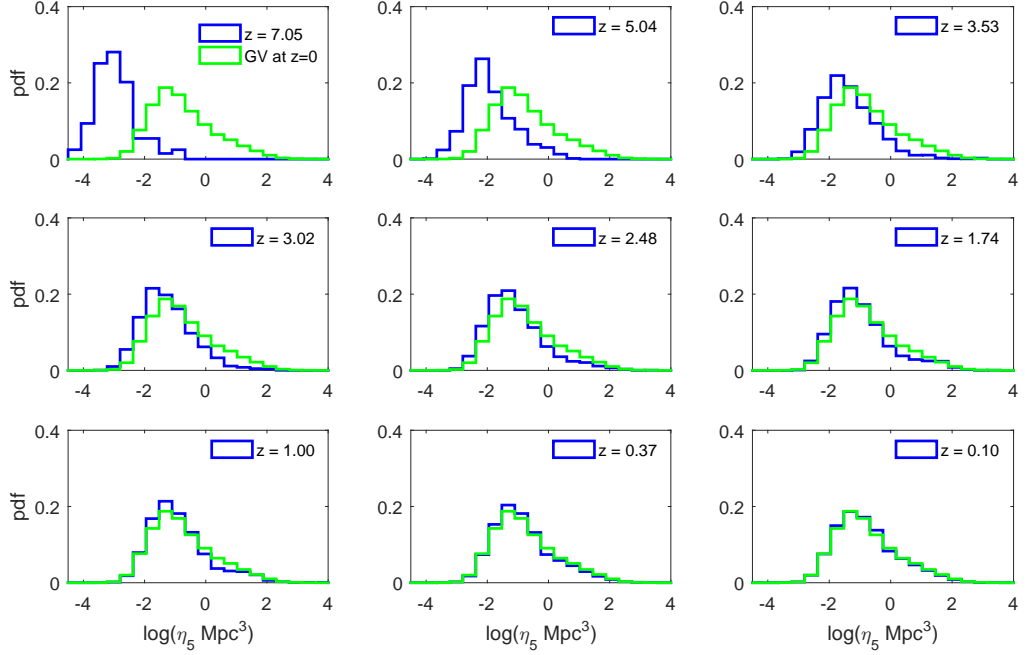


Figure 11. This shows the PDF of the local density of the GV progenitors at various redshifts. The PDF of the local density of the present-day GV galaxies are shown together in each panel for comparison.

complex regulation of star formation in GV progenitors.

The slope of the cold gas mass–halo mass relation for GV progenitors at various redshifts is determined through least-squares fitting, as shown in Figure 9. This slope evolves notably with redshift, decreasing from $z = 10$ to $z = 6$, then increasing slightly between $z = 6$ and $z = 2$, and rising more significantly at $z < 2$.

At $z > 6$, the weak dependence of cold gas mass on halo mass suggests that GV progenitors are in an early growth phase. During this time, cold gas availability is abundant, with accretion largely unhindered by halo mass constraints, fueling high star formation rates. The reduced correlation may also reflect the regulatory effects of significant AGN activity (Figure 2), which can limit gas accretion, particularly in massive halos.

Between $z = 6$ and $z = 2$, the dependency of cold gas mass on halo mass strengthens as interactions and feedback mechanisms increasingly regulate cold gas reservoirs. During this period, galaxy interactions peak, with about $\sim 25\%$ of GV progenitors experiencing interactions at $z = 2$, triggering starbursts and accelerating cold gas depletion. High-mass progenitors, however, manage to maintain their cold gas more effectively, allowing them to sustain star formation for longer periods. This marks a transitional era where halo properties begin to play a more prominent role in shaping cold gas availability.

At $z < 1$, cold gas reservoirs in GV progenitors deplete rapidly (Figure 5). Progenitors in low-mass halos are particularly susceptible to feedback effects like supernova-driven outflows and environmental quenching mechanisms such as ram pressure stripping, leading to rapid gas loss and quenching of star formation. In contrast, high-mass halos, with their deeper

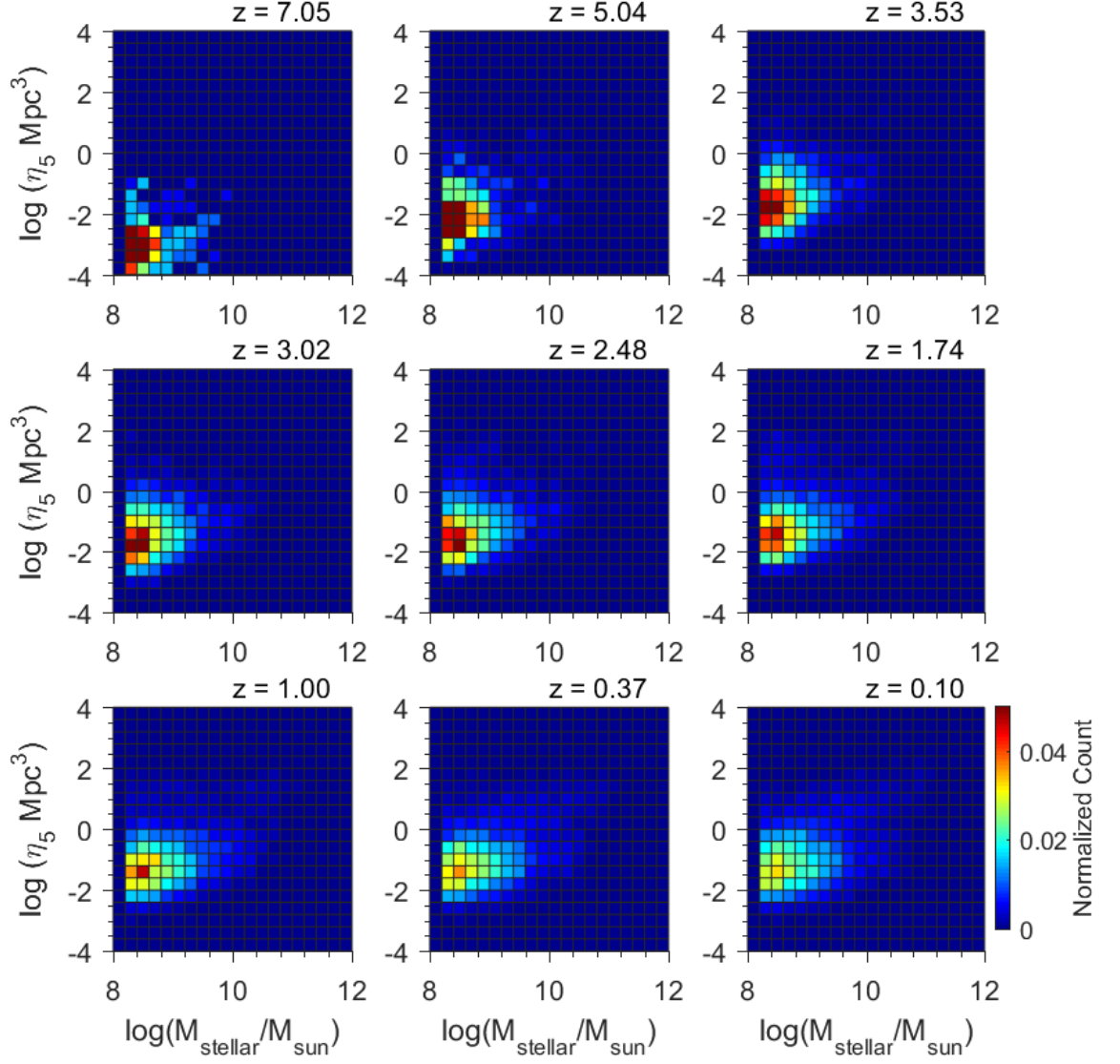


Figure 12. This shows the joint PDF of stellar mass and local density of the GV progenitors at different redshifts. The colour bar represents the magnitude of the joint PDF of stellar mass and local density.

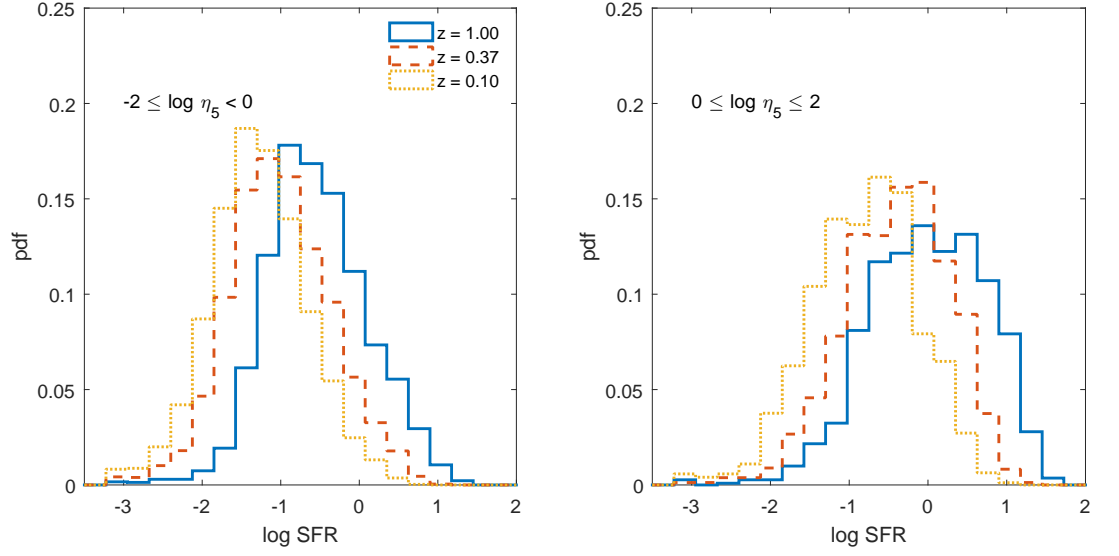


Figure 13. The two panels of this figure show the PDF of the SFR for the GV progenitors at $z = 0.1, 0.37, 1.00$ in low- and high- density regions.

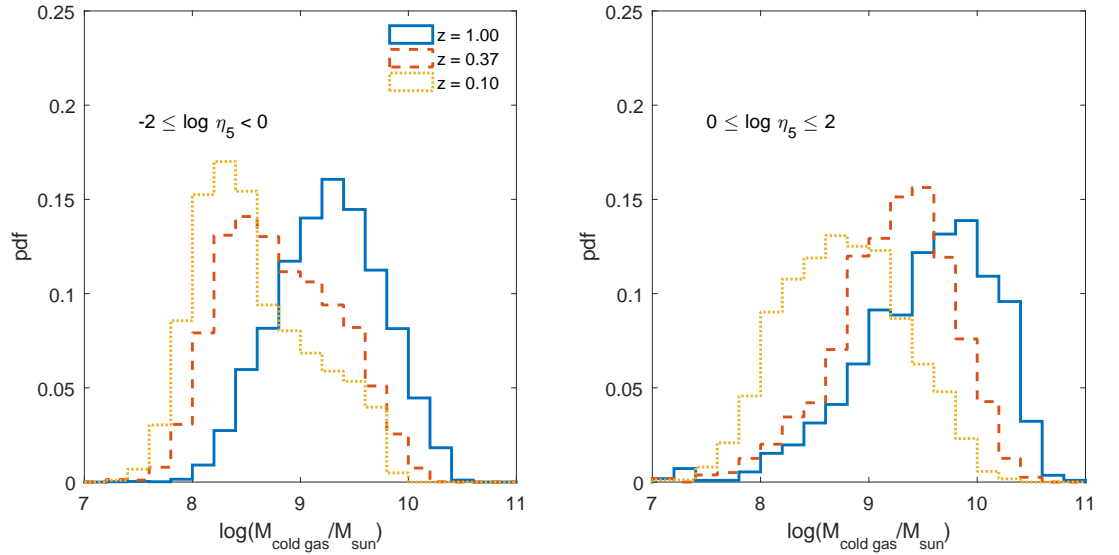


Figure 14. The left panel of this figure shows the PDF of the cold gas content for the GV progenitors residing at low-density regions at $z = 0.1, 0.37, 1.00$. The right panels shows the same but for the GV progenitors residing in the high density regions.

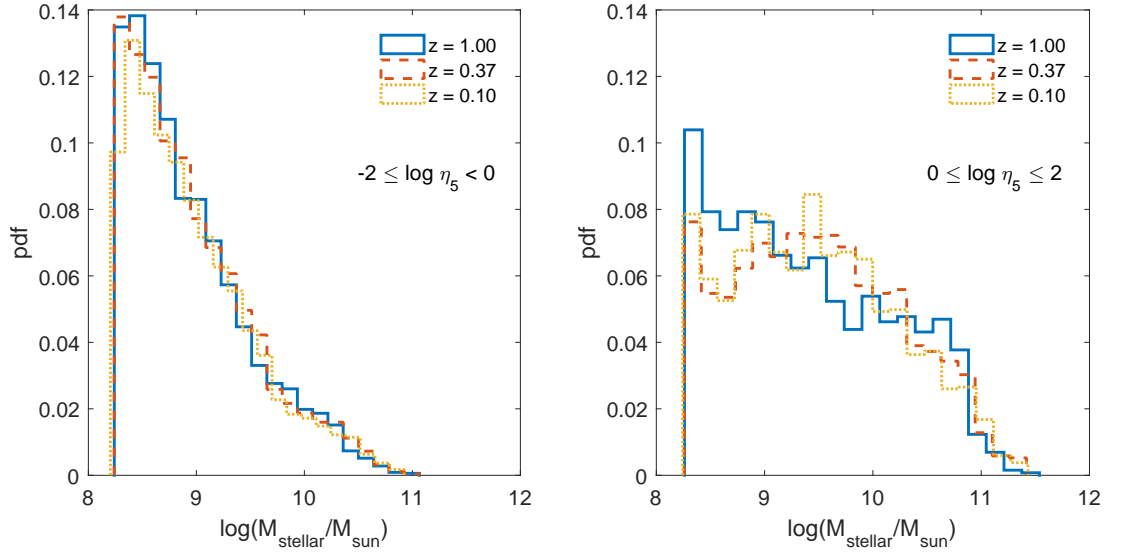


Figure 15. The left panel and right panel of this figure respectively show the PDF of the stellar mass for the GV progenitors residing at low-density and high-density regions. The results are shown for three different redshifts $z = 0.1, 0.37, 1.00$.

gravitational wells, better resist gas stripping and retain cold gas for longer durations. As GV progenitors increasingly migrate into intermediate- and high-density regions, environmental processes selectively strip cold gas from smaller halos, steepening the slope of the relation.

The sharp increase in slope at $z < 1$ reflects a divergence in progenitor evolution. The low-mass halos quench quickly, while high-mass halos continue to sustain star formation during this phase, highlighting the critical role of halo mass in late-stage galaxy evolution.

3.4 Roles of mass and local environment in the evolution of the progenitors of the present-day green valley galaxies

We examine the evolution of the stellar mass distribution for the progenitors of present-day GV galaxies in Figure 10. Each panel compares the stellar mass distribution of GV progenitors at different redshifts with that of present-day GV galaxies. The results reveal that the high-mass end of the stellar mass distribution gradually extends to larger values with decreasing redshift, reflecting the hierarchical growth of structures. This growth is driven by successive mergers of low-mass GV progenitors, which combine to form more massive galaxies over time. At lower redshifts ($z < 1$), stellar mass growth continues at a slower pace.

We compare the local density distributions of GV progenitors with present-day GV galaxies across different redshifts in Figure 11. The results show that GV progenitors gradually transition from low-density regions at high redshifts to moderate and high-density environments as redshift decreases. This shift becomes particularly pronounced at $z < 1$, where the migration into intermediate- and high-density regions exposes these galaxies to environmental quenching mechanisms. Despite this trend, the majority of GV progenitors still reside in low- to intermediate-density environments, even at lower redshifts. Additionally, the environmental conditions of GV progenitors exhibit only moderate changes at $z < 1$, suggesting that

while environment plays an increasing role in their evolution, many GV progenitors remain in less dense regions where quenching is less aggressive.

The joint PDF of stellar mass and local density for GV progenitors at various redshifts is presented in [Figure 12](#). The results again reveal a gradual migration of GV progenitors from low-density regions to intermediate- and high-density environments as redshift decreases. Until $z = 3$, the majority of GV progenitors are situated in low-density regions. Over time, as redshift decreases, these galaxies gradually migrate to higher-density environments, highlighting the role of environmental factors in their evolution. By $z < 1$, the more massive GV progenitors (with stellar masses exceeding $10^{10} M_{\text{sun}}$) are predominantly found in high-density environments where dynamical interactions and gas stripping suppress star formation, leading to a faster progression through the green valley phase. Despite this trend, most GV progenitors continue to reside in low- to intermediate-density regions and have stellar mass $< 10^{10} M_{\text{sun}}$.

In [Figure 13](#), [Figure 14](#) and [Figure 15](#), we analyze the evolution of SFR, cold gas content, and stellar mass in GV progenitors residing in low- and high-density environments. The two panels of [Figure 13](#) compare the PDFs of SFR for GV progenitors at $z = 0.1, 0.37$, and 1 in low- and high-density regions, respectively. Similarly, the panels of [Figure 14](#) present the cold gas distributions in GV progenitors for these environments. These figures reveal significant evolution in both SFR and cold gas reservoirs for GV progenitors at $z < 1$, regardless of their environments. A clear reduction in cold gas content and a suppression of SFR is observed with decreasing redshift. However, the PDFs show a more pronounced shift in high-density environments, indicating faster cold gas depletion and more rapid suppression of star formation in these regions. This provides important insights into the evolutionary pathways of GV progenitors. Low-mass progenitors evolve slowly in low-density regions, with their development shaped by gradual processes and slow gas depletion ([Figure 15](#)). High-mass progenitors in low-density environments also experience extended periods in the green valley, primarily driven by internal processes. In contrast, low-mass progenitors in high-density environments undergo rapid quenching due to external environmental factors whereas the high-mass progenitors hasten their entry into the green valley due to their capability of retaining cold gas for a longer duration ([Figure 15](#)).

3.5 Evolution of the main progenitor branches of the present-day green valley galaxies

our sample of GV progenitors may include a significant number of satellite galaxies which may bias the results in our analysis. In order to assess their influence, we also repeat some of our analysis considering only the main progenitor branches of the present day GV galaxies. We show the evolution of the AGN fraction in the main progenitor branches in [Figure 16](#). It shows that the evolution of the AGN fraction in the main progenitor branches is quite similar to [Figure 2](#). The similarities in [Figure 2](#) and [Figure 16](#) suggest that our primary sample of GV progenitors is not dominated by the satellite population. We note that a large number of satellites are excluded by a cut in the stellar mass ($\log(M_{\text{stellar}}/M_{\text{sun}}) \geq 8.3$) of our primary sample of GV progenitors. However, such a cut in the stellar mass would not exclude all the satellite galaxies. A slightly higher magnitude of the AGN fraction is observed in the main progenitor branches compared to the primary sample of GV progenitors at all redshifts $z > 2$ ([Figure 2](#) and [Figure 16](#)). This indicates that the AGN fraction in the GV progenitors are somewhat underestimated at higher redshifts due to the inclusion of the satellite population.

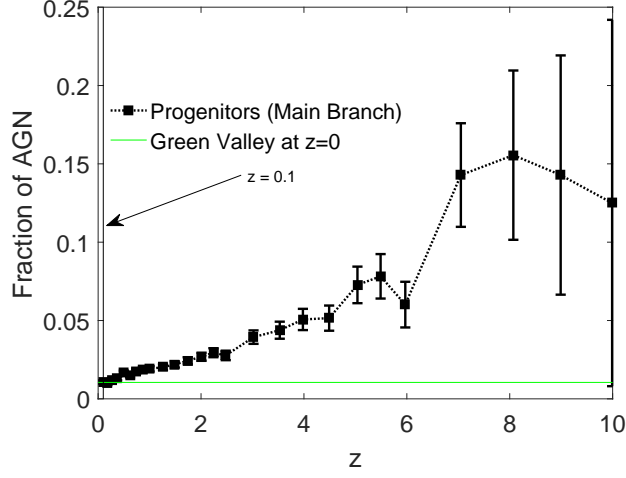


Figure 16. Same as Figure 2 but only for the main progenitor branches of the $z = 0$ GV galaxies.

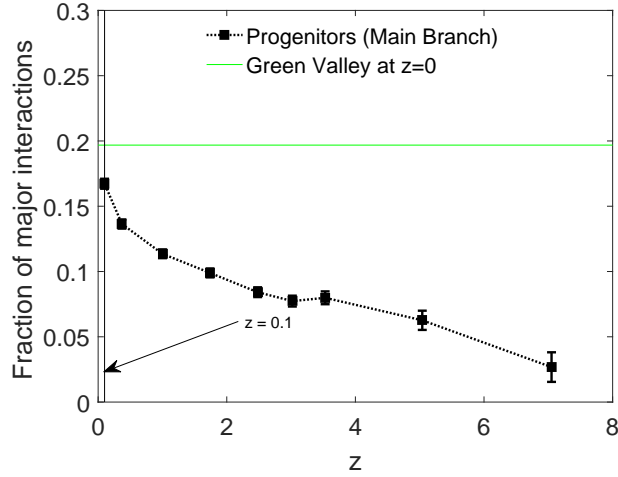


Figure 17. This shows the fraction of main progenitor branches of $z = 0$ GV galaxies in major pairs at different redshifts.

Both Figure 2 and Figure 16 show that AGN activity began to wane at intermediate redshifts ($2 < z < 6$) and diminish significantly at $z < 2$.

We also calculate the fraction of main progenitor branches in major pairs as a function of redshift in Figure 17. Interestingly, we do not find a declining trend in the fraction of main progenitor branches in major pairs at $z < 2$. In fact, the fraction of main progenitor branches in major pairs increases from $\sim 8\% - 9\%$ at $z = 2$ to $\sim 17\%$ at $z = 0.1$. This emphasizes the role of interactions in the evolution of the main progenitor branch even at smaller redshift.

We show the evolution of SFR and stellar mass in main progenitor branches for four $z = 0$ GV galaxies in Figure 18. The main progenitor branches of two massive GV galaxies in the two upper panel of this figure show steady rise in SFR until $z = 2$. The results for main

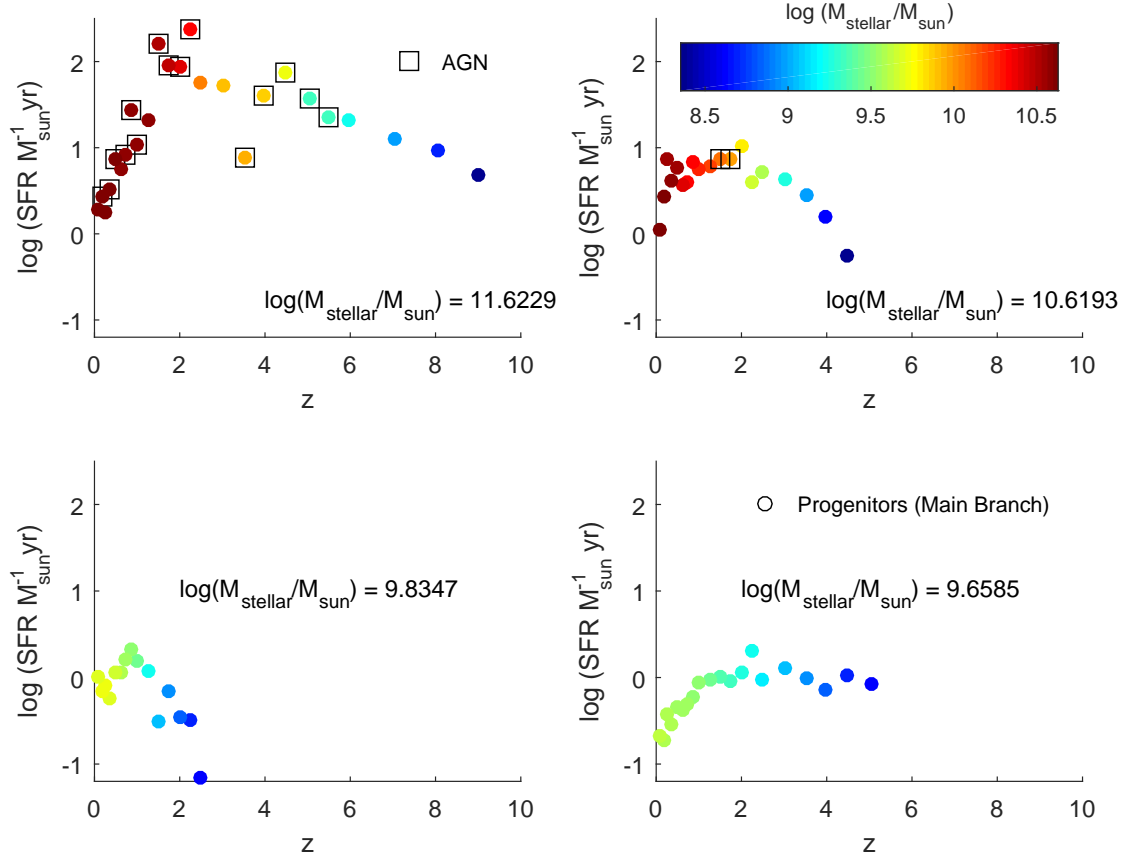


Figure 18. This figure shows the evolution of SFR and stellar mass in main progenitor branches for 4 present-day GV galaxies. The present stellar mass of these four $z = 0$ GV galaxies are mentioned in the respective panel. We mark the presence of AGN activity in the main progenitor branch at different redshift using rectangular boxes.

progenitor branches of two less massive GV galaxies are shown in the bottom two panels of this figure. We see that the SFR in the main progenitor branch of the low mass GV galaxies increase or remain unchanged with decreasing redshift before $z > 1$. Figure 18 shows that a dramatic decline in the SFR in the main progenitor branch is observed at $z < 1$ irrespective of the stellar mass of the present-day GV galaxies. Both rapid mass growth due to major mergers and onset of AGN activity likely play a significant role in suppressing the formation in the main progenitor branches of the two massive $z = 0$ GV galaxies. The main progenitor branches of the two low mass GV galaxies have lower SFR compared to the high mass GV galaxies. They experience a stronger environmental quenching at $z < 1$.

Finally, in Figure 19, we present the fraction of the main progenitor branches of present-day ($z = 0$) GV galaxies that entered or transitioned through the green valley at various redshifts. We find that most of the main progenitor branches of GV galaxies ($\sim 50\%$) entered the green valley at $z < 1$. Notably, a small subset ($\sim 5\%$) of the main progenitor branches

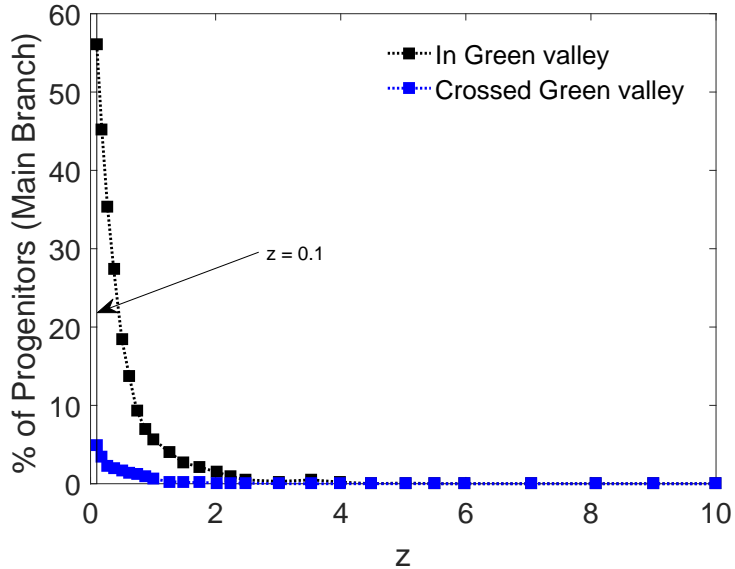


Figure 19. This figure shows the fraction of the main progenitor branches of the present day GV galaxies that entered or crossed the green valley at different redshift. It is interesting to note that a small fraction ($\sim 5\%$) of the main progenitor branches has already crossed the green valley and entered the red sequence by $z = 0.1$. These galaxies must have gone through some rejuvenation after $z = 0.1$ that helped them to reenter the present-day green valley.

had already crossed the green valley and joined the red sequence by $z = 0.1$. This suggests that these galaxies must have experienced some form of rejuvenation after $z = 0.1$, likely through processes such as gas accretion or minor mergers, which reignited star formation and allowed them to reenter the green valley by the present day. This highlights the dynamic and non-linear evolutionary pathways that galaxies can follow during their journey through the green valley.

4 Conclusions and Discussions

We investigate the evolution of the progenitors of the present-day GV galaxies across the redshift range $z = 10 - 0$ using data from the EAGLE simulations. At high redshift, most GV progenitors have stellar masses below $10^{10} M_{\text{sun}}$. They are gas-rich and actively forming stars (Figure 5, Figure 4 and Figure 10). At $z > 6$, their growth is dominated by the smooth accretion of cold gas and less influenced by interactions and mergers (Figure 3, Figure 17). 6%–12% of the GV progenitors shows AGN activity during this period (Figure 2). The AGN feedback during this time suppress star formation in these GV progenitors, moving them from the blue cloud into the green valley. The main progenitor branches of the GV galaxies exhibit a similar behaviour with a slightly higher fraction of AGN during this period (Figure 16). AGN activity starts to decline at intermediate redshifts ($2 < z < 6$) and drops significantly at $z < 2$. Only 2%–3% GV progenitors exhibit AGN activity at $z = 0.1$ (Figure 2, Figure 16).

GV progenitors gradually migrate from low-density to intermediate- and high-density environments with decreasing redshift (Figure 11, Figure 12). In high-density regions, inter-

actions and mergers between low-mass progenitors drive the formation of higher-mass progenitors ($> 10^{10} M_{\text{sun}}$). These interactions can trigger starbursts, depleting cold gas reservoirs, and accelerate their transition into the green valley. The fraction of interacting progenitors rises from $\sim 5\%$ at $z = 7$ to $\sim 25\%$ at $z = 2$ (Figure 3), emphasizing the critical role of galaxy interactions in shaping GV evolution. At $z < 2$, the fraction of interacting progenitors declines, indicating a diminished role for these processes in quenching star formation at lower redshifts. However, the fraction of the main progenitor branches of GV galaxies keeps increasing even at $z < 2$ (Figure 17) indicating the roles of interactions and mergers in their migration to the green valley. Most of the main progenitor branches ($\sim 50\%$) of the present-day GV galaxies enter the Green valley after $z < 1$. Around $\sim 5\%$ of the main progenitor branches of the GV galaxies cross the green valley to enter the red sequence by $z = 0.1$. These progenitors experience some kind of rejuvenation after $z = 0.1$ to reenter the green valley.

At $z > 2$, the stellar mass of progenitors and their host dark matter halos have a less decisive impact on star formation and quenching. However, at $z < 1$, tighter correlations between stellar mass and SFR (Figure 6, Figure 7), and halo mass and cold gas (Figure 8, Figure 9) content emerge, suggesting these factors become more influential. A sharp decline in cold gas content and a rapid suppression of star formation at $z < 1$ (Figure 5, Figure 4) highlight the growing importance of environmental processes in the evolution of GV progenitors. The evolution of GV progenitors is shaped by the interplay between environment and stellar mass. Secular processes dominate in low-density environments for lower-mass progenitors, while environmental quenching mechanisms prevail in high-density regions for massive progenitors. Once the universe entered a phase of accelerated expansion at low redshift ($z < 1$), interactions in low-density regions likely became much less frequent.

In our analysis, the evolution of green valley (GV) progenitors can be broadly divided into three distinct phases:

(i) Early growth phase ($z = 10$ to $z = 6$) during which GV progenitors have abundant cold gas, enabling efficient gas accretion and high star formation rates. They predominantly reside in low-density environments with minimal external quenching influences. AGN feedback plays a key regulatory role, particularly in massive progenitors, by moderating star formation activity.

(ii) Transition phase ($z = 6$ to $z = 2$) during which GV progenitors begin migrating toward intermediate- and high-density regions. Frequent galaxy interactions in dense environments trigger starbursts, drive AGN activity, and disrupt gas reservoirs. These processes enhance the correlation between cold gas mass and halo properties, as feedback and dynamical effects increasingly regulate the gas content.

(iii) Quenching phase ($z = 2$ to $z = 0$) which is marked by strong cold gas depletion and rapid suppression of star formation. Quenching becomes increasingly governed by environmental and mass-dependent processes, with high-density environments and internal mechanisms playing critical roles in halting star formation.

In the quenching phase, the evolution of GV progenitors is shaped by the interplay between mass and environmental density, leading to diverse trajectories. The low-mass GV progenitors in low-density environments evolve slowly, with moderate star formation sustained by less effective environmental quenching and gradual depletion of cold gas. The prolonged

green valley phase observed in these galaxies may result from the gradual influence of secular processes. The quenching in high-mass GV progenitors in low-density environments could be primarily governed by internal mechanisms, including AGN activity, mass quenching, morphological quenching, and bar quenching. This results in a prolonged residence in the green valley. On the other hand, the low-mass GV progenitors in high-density environments would experience rapid cold gas loss due to strong environmental quenching mechanisms, such as ram pressure stripping and galaxy harassment, leading to a quick transition through the green valley. High-mass GV progenitors in dense environments are likely quenched by a combination of internal feedback mechanisms (such as AGN feedback) and external environmental influences. It may be noted that our analysis excludes all the GV progenitors with $\log(M_{\text{stellar}}/M_{\text{sun}}) < 8.3$. Despite this, we find that the majority of GV progenitors are lower-mass galaxies ($< 10^{10} M_{\text{sun}}$) residing in low- to intermediate-density regions. As a result, their transition through the green valley is generally prolonged, contributing to the extended evolutionary journey of the present-day GV population.

It is important to discuss some caveats in our analysis. In this analysis, we focus exclusively on GV progenitors with stellar masses $\log(M_{\text{stellar}}/M_{\text{sun}}) \geq 8.3$ across the entire redshift range. This exclusion of progenitors with masses below $8.3 \times 10^8 M_{\text{sun}}$ introduces biases, particularly underestimating the contributions of low-mass progenitors to the overall evolution of GV galaxies. Low-mass progenitors, especially in low-density environments, are likely underrepresented in this study. These galaxies typically evolve more gradually, driven by secular processes and slower gas depletion. Their omission may lead to an overemphasis on rapid quenching mechanisms and interactions, skewing the evolutionary picture toward higher-mass systems. Moreover, low-mass progenitors in low-density environments often transition through the green valley more slowly due to less efficient quenching, and their exclusion could somewhat exaggerate the prevalence of rapid transitions. Additionally, low-mass galaxies are more sensitive to environmental effects such as ram pressure stripping and tidal interactions, particularly in high-density regions. Excluding them provides an incomplete understanding of how environmental quenching operates across the full mass spectrum. These biases will be more pronounced at higher redshifts, where progenitors tend to be less massive.

Finally, we compare our findings with previous studies utilizing both simulations and observations. Using COSMOS survey data, [99] report evidence of mergers in green valley (GV) galaxies at $z \sim 1.2$. [100] find that GV galaxies were preferentially more massive in the past. [101] propose a quasi-static picture where most GV galaxies were partially quenched in the distant past and are now experiencing a gradual decline in star formation. [72] identify multiple quenching mechanisms in GV galaxies, including truncation of gas supply followed by gradual depletion, and gas reservoir destruction during major mergers or AGN feedback. Using EAGLE simulations, [11] investigate galaxy colour evolution and find that most GV galaxies remain in the green valley for less than 2 Gyr, regardless of the quenching mechanism. [73] emphasize the environmental dependence of external quenching mechanisms in GV galaxies. Analyzing data from the Hyper Suprime-Cam Survey, [102] observe a strong mass dependence and mild environmental influence in the redshift evolution of GV galaxies. In the nearby universe, [78] use SDSS data to reveal that secular processes are more influential than environment-driven quenching in suppressing star formation in present-day GV galaxies. However, this analysis primarily focused on the higher mass green valley galaxies. [82], analyzing HST data, find that GV progenitors were more compact than present-day star-forming galaxies, indicating significant morphological evolution. [83] study GV galaxies in the nearby universe ($z \leq 0.11$) and conclude that their evolution is governed by distinct

mechanisms depending on the environment. Our findings align with several aspects of earlier studies while offering some nuanced insights into the evolution of galaxies in the green valley.

In conclusion, our study indicates that GV progenitors undergo a distinct evolutionary transition over cosmic time, shifting from AGN-dominated quenching at high redshifts ($6 \leq z < 10$) to interaction-driven evolution at intermediate redshifts ($2 \leq z < 6$), and finally to environmentally driven quenching at low redshifts ($0 \leq z < 2$). These processes, working in tandem with the progressive depletion of cold gas, shape the transformation of the GV population over cosmic time.

5 Acknowledgements

We thank an anonymous reviewer for the valuable comments and suggestions that helped us to improve the draft. BP acknowledges the support provided by IUCAA, Pune, through its associateship program. The authors extend their gratitude to the Virgo Consortium for providing public access to their simulation data. The EAGLE simulations were performed using the DiRAC-2 facility at Durham, managed by the ICC, and the PRACE facility Curie based in France at TGCC, CEA, Bruyères-le-Châtel.

6 Data availability

The EAGLE simulation data are publicly accessible at <https://icc.dur.ac.uk/Eagle/database.php>. Data generated in this study will be made available upon reasonable request to the authors.

References

- [1] I. Strateva, et al., *AJ*, **122**, 1861 (2001)
- [2] M. R. Blanton, et al., *ApJ*, **594**, 186 (2003)
- [3] E. F. Bell, D. H. McIntosh, N. Katz, M. D. Weinberg, *ApJS*, **149**, 289 (2003)
- [4] M. L. Balogh, I. K. Baldry, R. Nichol, C. Miller, R. Bower, K. Glazebrook, 2004, *ApJL*, **615**, L101 (2004)
- [5] I. K. Baldry, K. Glazebrook, J. Brinkmann, Ž. Ivezić, R. H. Lupton, R. C. Nichol, A. S. Szalay, *ApJ*, **600**, 681 (2004)
- [6] N. Menci, A. Fontana, E. Giallongo, & S. Salimbeni, *ApJ*, **632**, 49 (2005)
- [7] S. P. Driver, et al., *MNRAS*, **368**, 414 (2006)
- [8] A. Cattaneo, A. Dekel, J. Devriendt, B. Guiderdoni, & J. Blaizot, *MNRAS*, **370**, 1651 (2006)
- [9] A. Cattaneo, et al., *MNRAS*, **377**, 63 (2007)
- [10] E. Cameron, S. P. Driver, A. W. Graham, J. Liske, *ApJ*, **699**, 105 (2009)
- [11] J. W. Trayford, et al., *MNRAS*, **460**, 3925 (2016)
- [12] D. Nelson, et al., *MNRAS*, **475**, 624 (2018)
- [13] C. A. Correa, J. Schaye, & J. W. Trayford, *MNRAS*, **484**, 4401 (2019)
- [14] E. F. Bell, C. Wolf, K. Meisenheimer, H.-W. Rix, A. Borch, S. Dye, M. Kleinheinrich, et al., *ApJ*, **608**, 752 (2004)
- [15] B. J. Weiner, A. C. Phillips, S. M. Faber, C. N. A. Willmer, N. P. Vogt, L. Simard, K. Gebhardt, et al., *ApJ*, **620**, 595 (2005)

- [16] M. Kriek, A. van der Wel, P. G. van Dokkum, M. Franx, G. D. Illingworth, *ApJ*, **682**, 896 (2008)
- [17] G. B. Brammer, K. E. Whitaker, P. G. van Dokkum, D. Marchesini, I. Labbé, M. Franx, M. Kriek, et al., *ApJL*, **706**, L173 (2009)
- [18] S. M. Faber, C. N. A. Willmer, C. Wolf, D. C. Koo, B. J. Weiner, J. A. Newman, M. Im, et al., *ApJ*, **665**, 265 (2007)
- [19] P. Madau, H. C. Ferguson, M. E. Dickinson, M. Giavalisco, C. C. Steidel, & A. Fruchter, *MNRAS*, **283**, 1388 (1996)
- [20] T. K. Wyder, D. C. Martin, D. Schiminovich, M. Seibert, T. Budavári, M. A. Treyer, T. A. Barlow, et al., *ApJS*, **173**, 293 (2007)
- [21] P. F. Hopkins, L. Hernquist, T. J. Cox, D. Kereš, *ApJS*, **175**, 356 (2008)
- [22] B. Moore, N. Katz, G. Lake, A. Dressler, & A. Oemler, A., *Nature*, **379**, 613 (1996)
- [23] B. Moore, G. Lake, & N. Katz, N., *ApJ*, **495**, 139 (1998)
- [24] J. E. Gunn, & J. R. Gott, *ApJ*, **176**, 1 (1972)
- [25] M. L. Balogh, J. F. Navarro, & S. L. Morris, *ApJ*, **540**, 113 (2000)
- [26] R. B. Larson, B. M. Tinsley, & C. N. Caldwell, *ApJ*, **237**, 692 (1980)
- [27] R. S. Somerville, & J. R. Primack, *MNRAS*, **310**, 1087 (1999)
- [28] D. Kawata, & J. S. Mulchaey, *ApJL*, **672**, L103 (2008)
- [29] M. Geha, M. R. Blanton, R. Yan, J. L. Tinker, *ApJ*, **757**, 85 (2012)
- [30] A. Toomre, J. Toomre, *ApJ*, **178**, 623 (1972)
- [31] J. E. Barnes, L. Hernquist, *ApJ*, **471**, 115 (1996)
- [32] J. C. Mihos, L. Hernquist, *ApJ*, **464**, 641 (1996)
- [33] P. B. Tissera, R. Domínguez-Tenreiro, C., Sáiz A. Scannapieco, *MNRAS*, **333**, 327 (2002)
- [34] T. J. Cox, P. Jonsson, J. R. Primack, R. S. Somerville, *MNRAS*, **373**, 1013 (2006)
- [35] M. Montuori, P. Di Matteo, M. D. Lehnert, F. Combes, B. Semelin, *A&A*, **518**, A56 (2010)
- [36] J. M. Lotz, P. Jonsson, T. J. Cox, D. Croton, J. R. Primack, R. S. Somerville, K. Stewart, *ApJ*, **742**, 103 (2011)
- [37] P. Torrey, T. J. Cox, L. Kewley, L. Hernquist, *ApJ*, **746**, 108 (2012)
- [38] P. F. Hopkins, T. J. Cox, L. Hernquist, D. Narayanan, C. C. Hayward, N. Murray, *MNRAS*, **430**, 1901 (2013)
- [39] F. Renaud, F. Bournaud, K. Kraljic, P.-A. Duc, *MNRAS*, **442**, L33 (2014)
- [40] F. Renaud, F. Bournaud, P.-A. Duc, *MNRAS*, **446**, 2038 (2015)
- [41] J. Moreno, P. Torrey, S. L. Ellison, D. R. Patton, A. F. L. Bluck, G. Bansal, L. Hernquist, *MNRAS*, **448**, 1107 (2015)
- [42] J. Moreno, P. Torrey, S. L. Ellison, D. R. Patton, C. Bottrell, A. F. L. Bluck, M. H. Hani, et al., *MNRAS*, **503**, 3113 (2021)
- [43] F. Renaud, O. Segovia Otero, O. Agertz, *MNRAS*, **516**, 4922 (2022)
- [44] A. Das, B. Pandey, S. Sarkar, *RAA*, **23**, 115018 (2023)
- [45] R. B. Larson, B. M. Tinsley, *ApJ*, **219**, 46 (1978)
- [46] E. J. Barton, M. J. Geller, S. J. Kenyon, *ApJ*, **530**, 660 (2000)

- [47] D. G. Lambas, P. B. Tissera, M. S. Alonso, G. Coldwell, MNRAS, **346**, 1189 (2008)
- [48] M. S. Alonso, P. B. Tissera, G. Coldwell, D. G. Lambas, MNRAS, **352**, 1081 (2004)
- [49] B. Nikolic, H. Cullen, P. Alexander, MNRAS, **355**, 874 (2004)
- [50] D. F. Woods, M. J. Geller, E. J. Barton, AJ, **132**, 197 (2006)
- [51] D. F. Woods, M. J. Geller, AJ, **134**, 527 (2007)
- [52] E. J. Barton, J. A. Arnold, A. R. Zentner, J. S. Bullock, R. H. Wechsler, ApJ, **671**, 1538 (2007)
- [53] S. L. Ellison, D. R. Patton, L. Simard, A. W. McConnachie, AJ, **135**, 1877 (2008)
- [54] S. L. Ellison, D. R. Patton, L. Simard, A. W. McConnachie, I. K. Baldry, J. T. Mendel, MNRAS, **407**, 1514 (2010)
- [55] D. F. Woods, M. J. Geller, M. J. Kurtz, E. Westra, D. G. Fabricant, I. Dell’Antonio, AJ, **139**, 1857 (2010)
- [56] D. R. Patton, S. L. Ellison, L. Simard, A. W. McConnachie, J. T. Mendel, MNRAS, **412**, 591 (2011)
- [57] J. K. Barrera-Ballesteros, S. F. Sánchez, B. García-Lorenzo, J. Falcón-Barroso, D. Mast, R. García-Benito R., B. Husemann, et al., A&A, **579**, A45 (2015)
- [58] M. D. Thorp, S. L. Ellison, H.-A. Pan, L. Lin, D. R. Patton, A. F. L. Bluck, D. Walters, et al., MNRAS, **516**, 1462 (2022)
- [59] E. A. Shah, J. S. Kartaltepe, C. T. Magagnoli, I. G. Cox, C. T. Wetherell, B. N. Vanderhoof, K. C. Cooke, et al., ApJ, **940**, 4 (2022)
- [60] A. Das, B. Pandey, S. Sarkar S., RAA, **23**, 025016 (2022)
- [61] M. Martig, F. Bournaud, R. Teyssier, & A. Dekel, ApJ, **707**, 250 (2009)
- [62] Y. Birnboim, & A. Dekel, MNRAS, **345**, 349 (2003)
- [63] D. Kereš , N. Katz, D. H. Weinberg, & R. Davé , MNRAS, **363**, 2 (2005)
- [64] A. Dekel, & Y. Birnboim, MNRAS, **368**, 2 (2006)
- [65] J. M. Gabor, R. Davé , K. Finlator, & B. D. Oppenheimer, MNRAS, **407**, 749 (2010)
- [66] Y.-. jie Peng ., A. Renzini, MNRAS, **491**, L51 (2020)
- [67] K. L. Masters, M. Mosleh, A. K. Romer, R. C. Nichol, S. P. Bamford, K. Schawinski, C. J. Lintott, et al., MNRAS, **405**, 783 (2010)
- [68] T. J. Cox, J. Primack, P. Jonsson, & R. S. Somerville, ApJL, **607**, L87 (2004)
- [69] N. Murray, E. Quataert, & T. A. Thompson, ApJ, **618**, 569 (2005)
- [70] V. Springel, T. Di Matteo, & L. Hernquist, MNRAS, **361**, 776 (2005)
- [71] J. C. Mihos, & L. Hernquist, ApJL, **431**, L9 (1994)
- [72] K. Schawinski, C. M. Urry, B. D. Simmons, L. Fortson, S. Kaviraj, W. C. Keel, C. J. Lintott, et al., MNRAS, **440**, 889 (2014)
- [73] V. Coenda, H. J. Martínez, H. Muriel, MNRAS, **473**, 5617 (2018)
- [74] M. N. Bremer, S. Phillipps, L. S. Kelvin, R. De Propriis, R. Kennedy, A. J. Moffett, S. Bamford, et al., MNRAS, **476**, 12 (2018)
- [75] J. Angthopo, I. Ferreras, J. Silk, MNRAS, **488**, L99 (2019)
- [76] J. Angthopo, I. Ferreras, J. Silk, MNRAS, **495**, 2720 (2020)
- [77] B. Pandey, MNRAS, **499**, L31 (2020)

- [78] A. Das, B. Pandey, S. Sarkar, JCAP, **06**, 045 (2021)
- [79] S. Sarkar, B. Pandey, A. Das, JCAP, **03**, 024 (2022)
- [80] L. Quilley, V. de Lapparent, A&A, **666**, A170 (2022)
- [81] G. Noirot, M. Sawicki, R. Abraham, M. Bradač, K. Iyer, T. Moutard, C. Pacifici, et al., MNRAS, **512**, 3566 (2022)
- [82] V. Estrada-Carpenter, C. Papovich, I. Momcheva, G. Brammer, R. C. Simons, N. J. Cleri, M. Gialvalisco, et al., ApJ, **951**, 115 (2023)
- [83] D. Brambila, P. A. A. Lopes, A. L. B. Ribeiro, A. Cortesi, MNRAS, **523**, 785 (2023)
- [84] B. Pandey, Astronomy and Computing, **44**, 100725 (2023)
- [85] B. Pandey, MNRAS, **530**, 4550 (2024)
- [86] T. Pun, Computer Graphics and Image Processing, **16**, 210 (1981)
- [87] J. N. Kapur, P. K. Sahoo, A. K. C. Wong, Computer Vision, Graphics and Image processing, **29**, 273 (1985)
- [88] Schaye J et. al., MNRAS, **446**, 521 (2015)
- [89] McAlpine S., Helly J C., Schaller M., Trayford J W. et. al., A&A, **72**, 15 (2016)
- [90] Crain R A et. al., MNRAS, **450**, 1937 (2015)
- [91] Planck Collaboration et. al., A&A, **571**, A1 (2014)
- [92] Doi M et. al., AJ, **139**, 1628 (2010)
- [93] Trayford J W et. al., MNRAS, **452**, 2879 (2015)
- [94] Casertano S & Hut P., ApJ, **80**, 298 (1985)
- [95] Baldwin J A., Phillips M M., Terlevich R., PASP **5**, 93 (1981)
- [96] McAlpine, S. et al., MNRAS, **494**, 5713 (2020)
- [97] Shakura, N, J & Sunyaev, R, A., A&A, **24**, 337 (1973)
- [98] Das A., Pandey B., Sarkar S., RAA, **11** 23 (2023)
- [99] K. Bundy, C. Scarlata, C. M. Carollo, R. S. Ellis, N. Drory, P. Hopkins, M. Salvato, et al., ApJ, **719**, 1969
- [100] T. S. Gonçalves, D. C. Martin, K. Menéndez-Delmestre, T. K. Wyder, A. Koekemoer, ApJ, **759**, 67 (2012)
- [101] S. Salim, Serbian Astronomical Journal, **189**, 1 (2014)
- [102] H.-Y. Jian, L. Lin, Y. Koyama, I. Tanaka, K. Umetsu, B.-C. Hsieh, Y. Higuchi, et al., ApJ, **894**, 125 (2020)